

# A Neuromorphic Device Implemented on a Salmon-DNA Electrolyte and its Application to Artificial Neural Networks

Dong-Ho Kang, Jeong-Hoon Kim, Seyong Oh, Hyung-Youl Park, Sreekantha Reddy Dugasani, Beom-Seok Kang, Changhwan Choi, Rino Choi, Sungjoo Lee, Sung Ha Park, Keun Heo, and Jin-Hong Park\*


A bioinspired neuromorphic device operating as synapse and neuron simultaneously, which is fabricated on an electrolyte based on  $\text{Cu}^{2+}$ -doped salmon deoxyribonucleic acid (S-DNA) is reported. Owing to the slow  $\text{Cu}^{2+}$  diffusion through the base pairing sites in the S-DNA electrolyte, the synaptic operation of the S-DNA device features special long-term plasticity with negative and positive nonlinearity values for potentiation and depression ( $\alpha_p$  and  $\alpha_d$ ), respectively, which consequently improves the learning/recognition efficiency of S-DNA-based neural networks. Furthermore, the representative neuronal operation, “integrate-and-fire,” is successfully emulated in this device by adjusting the duration time of the input voltage stimulus. In particular, by applying a  $\text{Cu}^{2+}$  doping technique to the S-DNA neuromorphic device, the characteristics for synaptic weight updating are enhanced ( $|\alpha_p|$ : 31→20,  $|\alpha_d|$ : 11→18, weight update margin: 33→287 nS) and also the threshold conditions for neuronal firing (amplitude and number of stimulus pulses) are modulated. The improved synaptic characteristics consequently increase the Modified National Institute of Standards and Technology (MNIST) pattern recognition rate from 38% to 44% (single-layer perceptron model) and from 89.42% to 91.61% (multilayer perceptron model). This neuromorphic device technology based on S-DNA is expected to contribute to the successful implementation of a future neuromorphic system that simultaneously satisfies high integration density and remarkable recognition accuracy.

(series and linear processing).<sup>[1–3]</sup> Under this technical circumstance, a neuromorphic computing technology featuring parallel and nonlinear processing has been recently proposed to achieve an efficient computing platform for informal data.<sup>[4,5]</sup> Neuromorphic computing is performed on the basis of a hardware neural network (HNN),<sup>[6–8]</sup> which conceptually mimics a biological neural network consisting of synapses and neurons.<sup>[9,10]</sup> Accordingly, many studies aimed at implementing the HNN have been attempted by fabricating artificial synapse and neuron device arrays.<sup>[11–13]</sup> Although complementary metal-oxide semiconductor (CMOS) circuit techniques have achieved synaptic and neural functions,<sup>[12,14,15]</sup> a large number of CMOS transistors are required for the synapse and neuron circuits (10 transistors per synapse<sup>[16]</sup> and 5 transistors per neuron<sup>[17]</sup>). However, when such a large number of devices are integrated into an HNN system, they will cause significant problems such as high power consumption and low synapse/neuron packing density.<sup>[1,10,18,19]</sup> Therefore, it is essential to develop synaptic and neural devices that are highly efficient in energy consumption and can be integrated at a high density.

In the emerging “Big Data” era, it is challenging to handle large amounts of informal data, such as characters, images, sounds, and other unstructured data formats using current computing technology based on von Neumann architecture

Dr. D.-H. Kang, J.-H. Kim, S. Oh, Dr. H.-Y. Park, B.-S. Kang, Dr. K. Heo, Prof. J.-H. Park  
Department of Electrical and Computer Engineering  
Sungkyunkwan University  
Suwon 16419, Korea  
E-mail: jhpark9@skku.edu

Dr. D.-H. Kang  
School of Electrical and Electronic Engineering  
Nanyang Technological University  
50 Nanyang Avenue, 639798 Singapore, Singapore

 The ORCID identification number(s) for the author(s) of this article can be found under <https://doi.org/10.1002/advs.201901265>.

© 2019 The Authors. Published by WILEY-VCH Verlag GmbH & Co. KGaA, Weinheim. This is an open access article under the terms of the Creative Commons Attribution License, which permits use, distribution and reproduction in any medium, provided the original work is properly cited.

DOI: 10.1002/advs.201901265

Dr. S. R. Dugasani, Prof. S. H. Park  
Department of Physics  
Sungkyunkwan University  
Suwon 440-746, South Korea

Prof. C. Choi  
Division of Materials Science and Engineering  
Hanyang University  
Seoul 133–791, South Korea

Prof. R. Choi  
Material Science and Engineering  
Inha University  
Incheon 402–751, South Korea

Prof. S. Lee, Prof. J.-H. Park  
SKKU Advanced Institute of Nanotechnology (SAINT)  
Sungkyunkwan University  
Suwon 440–746, South Korea

Since Jo et al.<sup>[20]</sup> reported artificial synaptic behaviors, such as long-term potentiation/depression (LTP/LTD), in a Si/Ag-based memristor device in 2010, two-terminal memristive devices, such as phase-change random-access memory (PCRAM),<sup>[16,21,22]</sup> resistive-switching random-access memory (ReRAM),<sup>[23–25]</sup> and conductive bridge random-access memory (CBRAM) devices<sup>[26,27]</sup> have been studied actively as promising synaptic and neural devices for HNNs. Such devices could gradually change the conductance of the path of current according to input voltage pulses,<sup>[16,21–27]</sup> thereby allowing for the implementation of the functional operation of a synapse within a unit device. In particular, studies on memristive synapses have demonstrated that high-density HNNs can be constructed via fabrication in a crossbar point array structure.<sup>[28,29]</sup> Recently,  $\text{HfO}_x$ ,<sup>[30]</sup>  $\text{TaO}_x$ ,<sup>[31,32]</sup> or  $\text{TiO}_x$ ,<sup>[33,34]</sup> based ReRAM devices and  $\text{Ge}_2\text{Sb}_2\text{Te}_5$ -<sup>[16,35,36]</sup> or Mott-insulator<sup>[37]</sup> based PCRAM devices have successfully emulated synaptic dynamics, such as LTP/LTD characteristics and excitatory/inhibitory postsynaptic currents (EPSC/IPSC). Prezioso et al.<sup>[38]</sup> fabricated a neural network based on an  $\text{Al}_2\text{O}_3/\text{TiO}_x$  memristor crossbar point array and demonstrated successful pattern classification of  $3 \times 3$  binary images. In addition, PCRAM devices could emulate firing and relaxation functionalities of biological neurons owing to easy transition between insulator and metal. Tuma et al.<sup>[39]</sup> and Adda et al.<sup>[40]</sup> demonstrated a PCRAM-based neuron device with a basic neural function “integrate and fire,” subsequently presenting the possibility of simplifying the neuronal circuit to a unit device level. Very recently, a few studies that explore implementation of both synaptic and neuronal operations in one device have been reported.<sup>[35,36,39,40]</sup> In particular, Wang et al.<sup>[41]</sup> successfully built a fully memristive neural network through the integration of diffusive memristor ( $\text{Ag}/\text{SiO}_2/\text{Ag}/\text{Ag}$ ) neurons and drift memristor ( $\text{Ta}/\text{HfO}_x/\text{Pd}$ ) synapses, where they then demonstrated an unsupervised synaptic weight updating and a pattern classification by their fully memristive neural network.

Herein, we report a bio-inspired neuromorphic device operating as synapse and neuron simultaneously that is fabricated on a  $\text{Cu}^{2+}$ -doped salmon deoxyribonucleic acid (S-DNA) electrolyte. Owing to the slow  $\text{Cu}^{2+}$  diffusion through the base pairing sites in the S-DNA, the S-DNA device presents the special synaptic characteristic (LTP characteristic with negative nonlinearity), which consequently improves the accuracy of numerical digit pattern recognition of S-DNA-based neural network. In addition, this S-DNA device successfully emulates the integrate-and-fire behavior of a neuron. As the S-DNA synaptic and neural operations are based on Cu redox reactions ( $\text{Cu} \leftrightarrow \text{Cu}^{2+} + 2 e^-$ ), we discuss how the  $\text{Cu}^{2+}$  doping applied to the S-DNA electrolyte influences the synaptic and neural operating characteristics, respectively, in terms of: i) the nonlinearity and weight update margin of LTP/LTD characteristics and ii) the threshold condition of firing phenomenon. We then predict the accuracy of MNIST pattern recognition with respect to the number of learning steps, where a single-layer ANN structure (or a multilayer ANN structure for +NeuroSim simulator) and a back-propagation weight update algorithm are applied.

In a biological synapse, neurotransmitters are released from a presynaptic neuron. They then diffuse toward a postsynaptic neuron when an active signal reaches the presynaptic neuron.

Subsequently, the neurotransmitters are combined with receptors at the postsynaptic neuron, generating a postsynaptic signal.<sup>[42–44]</sup> As shown in **Figure 1a**, the signal transportation mechanism of the S-DNA device resembles that of the biological synapse. When a presynaptic spike signal ( $V_{\text{pre}}$ ) is applied to the Cu/Ti electrode, an electric-field-assisted diffusion of  $\text{Cu}^{2+}$  occurs between Cu/Ti and Pt electrodes. The diffused  $\text{Cu}^{2+}$  adjust the conductivity of the S-DNA device (synapse weight) by contributing to the formation of a Cu filament. Here, a Ti buffer layer was inserted at the Cu/S-DNA interface to improve the operating stability of the S-DNA device.<sup>[45]</sup> The buffer layer is expected to reduce the: i)  $\text{Cu}^{2+}$  diffusion rate into the S-DNA and ii) activation energy for the formation of the Cu filament. To understand the diffusion mechanism of  $\text{Cu}^{2+}$  in the S-DNA electrolyte in detail, we performed Raman spectroscopy analysis and Fourier-transform infrared spectroscopy (FT-IR) analyses. **Figure 1b** shows the Raman spectra measured on  $\text{Cu}^{2+}$ -doped S-DNA films with various concentrations (0, 0.1, and  $1 \times 10^{-3}$  M). In the spectral range from 600 to  $1400 \text{ cm}^{-1}$ , we observed eight Raman peaks. Here, the four Raman peaks between  $786$  and  $1095 \text{ cm}^{-1}$  indicate the vibration mode of the backbone of S-DNA,<sup>[46,47]</sup> and other Raman peaks (from  $1248$  to  $1375 \text{ cm}^{-1}$ ) are related to the S-DNA base pairs of cytosine (C), adenine (A), thymine (T), and guanine (G).<sup>[46,47]</sup> The Raman peak intensities monotonically decreased with increasing  $\text{Cu}^{2+}$  concentrations. In particular, the intensity decrease in the Raman peaks for the base pairs was more severe than that for backbone peaks. As the  $\text{Cu}^{2+}$  concentration increased from 0 to  $1 \times 10^{-3}$  M, the Raman peak intensities related to the S-DNA backbone and base pairs decreased by  $\approx 18\%$  and  $40\%$ , respectively, as shown in **Figure 1c**.

Similarly, in the FT-IR analysis shown in **Figure S3** in the Supporting Information, we confirmed that the FT-IR peak intensities related to the S-DNA base pairs were reduced by  $\text{Cu}^{2+}$  doping. This is because  $\text{Cu}^{2+}$  ions are preferably bound at the base pairing sites, thereby influencing the S-DNA molecular structure.<sup>[48]</sup> The binding of  $\text{Cu}^{2+}$  to the S-DNA molecule is graphically illustrated in **Figure 1d**. These  $\text{Cu}^{2+}$  ions are, thus, expected to move through the base pairs in the S-DNA molecule, enabling conductive filament-based switching. We then investigated the postsynaptic current characteristics of the S-DNA device to confirm its feasibility as a synaptic device. **Figure 1e,f** shows postsynaptic current change ( $\Delta\text{PSC}$ ) in the undoped S-DNA device, where we applied excitatory ( $V_{\text{pre}} = 4, 4.5, \text{ and } 5 \text{ V}$ ) and inhibitory ( $V_{\text{pre}} = -4, -4.5, \text{ and } -5 \text{ V}$ ) pulses with a duration time ( $t_d$ ) of 100 ms, respectively. The amplitude of the excitatory and inhibitory pulses was determined by the following procedure: i) we experimentally confirmed the set and reset voltages ( $V_{\text{SET}}$  and  $V_{\text{RESET}}$ ) of the S-DNA devices (**Figure S4**, Supporting Information); ii) we then selected three different pulse amplitudes near the  $V_{\text{SET}}$  and  $V_{\text{RESET}}$  values. Here, the chosen amplitudes for the excitatory pulses were 4, 4.5, and 5 V, and the ones for the inhibitory pulses were  $-4, -4.5, \text{ and } -5 \text{ V}$  because the  $V_{\text{SET}}$  and  $V_{\text{RESET}}$  were 4.5 and  $-4.5 \text{ V}$ , respectively. The excitatory postsynaptic current (EPSC) value increased to 7.2 nA after applying the +4 V pulse, whereas the inhibitory postsynaptic current (IPSC) induced by the  $-4 \text{ V}$  pulse decreased to  $-2.7 \text{ nA}$ . Moreover, the EPSC and IPSC values could be controlled by adjusting the pulse amplitude.

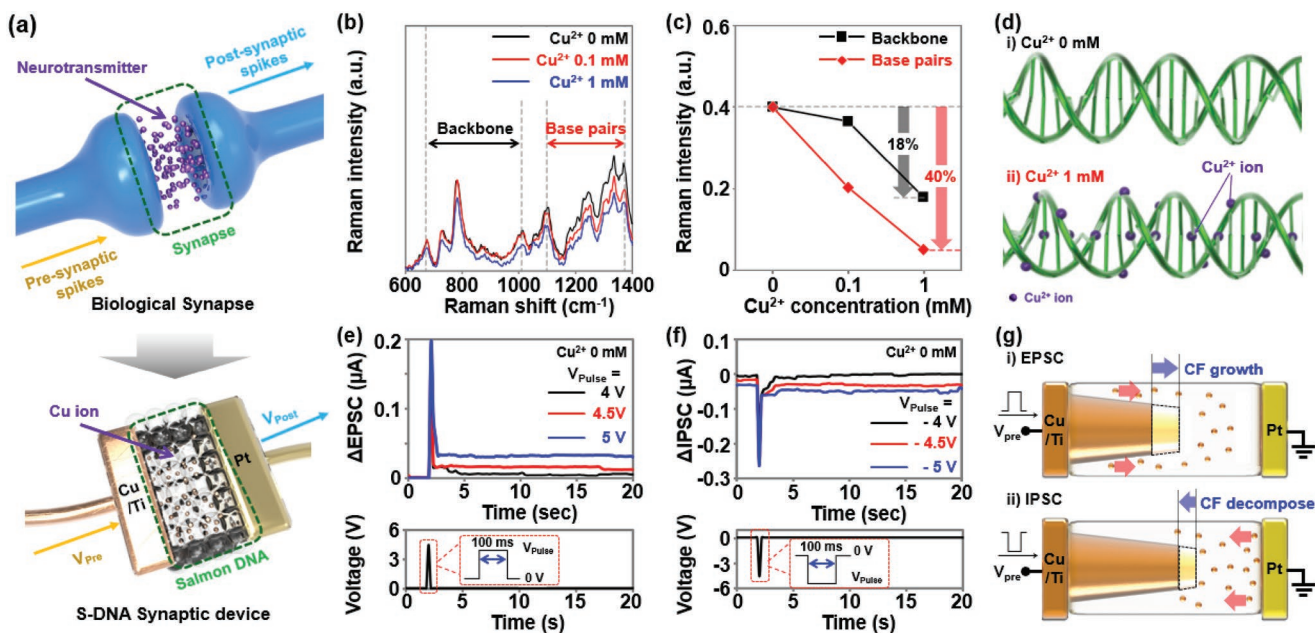


**Figure 1.** a) Schematic of biological synapse (top) and S-DNA synaptic device (bottom). b) Raman spectra of Cu<sup>2+</sup>-doped S-DNA films with various concentrations (0, 0.1, and 1 × 10<sup>-3</sup> M), and c) Raman intensities extracted from the spectra. d) Graphical illustration presenting the intercalation of Cu<sup>2+</sup> in the 0 × 10<sup>-3</sup> M (up) and 1 × 10<sup>-3</sup> M (down) Cu<sup>2+</sup>-doped S-DNA molecules. e) PSC response of S-DNA device induced by an excitatory voltage pulse with magnitudes of 4 V (black), 4.5 V (red), or 5 V (blue). f) PSC response of S-DNA synaptic device induced by an inhibitory voltage pulse with magnitudes of -4 V (black), -4.5 V (red), or -5 V (blue). Here, the duration time (*t<sub>d</sub>*) of the excitatory/inhibitory voltage pulses was 100 ms. g) Illustration showing conductive filament growth (up)/decomposition (down) by excitatory/inhibitory voltage pulses.

When increasing the amplitude of the excitatory pulse from 4 to 5 V, the EPSC value varied from 7.2 to 37.1 nA. Similarly, the ΔIPSC value decreased from -2.7 to -46.6 nA when the amplitude of the inhibitory pulse reduced to -5 V. The EPSC and IPSC characteristics of the S-DNA device can be explained by the growth and decomposition of Cu filament by the presynaptic spike signal (*V<sub>pre</sub>*), respectively, as illustrated in Figure 1g. When an excitatory *V<sub>pre</sub>* is applied to the Cu/Ti electrode, Cu<sup>2+</sup> ions diffuse into the S-DNA electrolyte and then a Cu filament starts growing from the Cu surface through the reduction process ( $\text{Cu}^{2+} + 2\text{e}^- \rightarrow \text{Cu}$ ). In contrast, an inhibitory *V<sub>pre</sub>* will lead to the oxidation of the Cu filament ( $\text{Cu} \rightarrow \text{Cu}^{2+} + 2\text{e}^-$ ), resulting in the decomposition of the filament in the S-DNA film.

The S-DNA device was investigated in more detail in terms of its long-term synaptic plasticity, such as its LTP/LTD characteristics. Figure 2a presents the LTP/LTD characteristics of the S-DNA device, to which we applied a series of 15 excitatory/inhibitory pulses (*V<sub>pre</sub>* = 4.5 V/-4.5 V and *t<sub>d</sub>* = 100 ms). Here, the amplitudes of the excitatory and inhibitory pulses were chosen on the basis of the set and reset voltages of the S-DNA device. As the excitatory pulses were applied, the current level was potentiated gradually from 1.7 to 52.1 nA. After that, the current level was depressed by the inhibitory pulses, eventually recovering to its initial level. From the LTP/LTD characteristic curves shown in Figure 2b, we extracted nonlinearity factors ( $\alpha$ ) and weight update margins ( $\Delta G = G_{\text{max}} - G_{\text{min}}$ ). Here, the blue dotted lines indicate ideal LTP/LTD curves ( $\alpha = 1$ ) and the circle symbol shows the experimental conductance data. The conductance values were fitted by using the equations  $G = B(1 - e^{P/A}) + G_{\text{min}}$  and  $G = -B(1 - e^{(P - P_{\text{max}})/A}) + G_{\text{min}}$ , where

*B* is a fitting factor, *P* is the pulse number, and *A* is the nonlinearity of potentiation ( $\alpha_p$ ) and depression ( $\alpha_d$ ). After fitting the data, we confirmed a special potentiation characteristic with a negative nonlinearity value in the S-DNA device. Typical synaptic devices have an LTP curve with a positive nonlinearity value (e.g., ReRAM and PCRAM).<sup>[21–28]</sup> The extraordinary LTP/LTD profiles with opposite nonlinearity values (negative  $\alpha_p$  and positive  $\alpha_d$ ) can be explained by the harsh Cu<sup>2+</sup> diffusion condition in the S-DNA electrolyte owing to the relatively lower number of defective sites. For easier understanding, we illustrated two operating mechanisms for the S-DNA device, as shown in Figure 2c. When the 1st to 7th excitatory pulses are transmitted (Case I in LTP), more Cu<sup>2+</sup> ions from the Cu electrode diffuse through the base pairing sites of the S-DNA to the Pt electrode and subsequently increase the conductance of the S-DNA device.<sup>[49,50]</sup> Here, owing to the slow diffusion of the Cu<sup>2+</sup> in the S-DNA electrolyte, the conductance value is predicted to slowly increase until the Cu<sup>2+</sup> reacted with the electrons coming from the Pt-side and a Cu filament is subsequently formed on the Cu-side.<sup>[50]</sup> After forming a Cu filament partially on the Cu-side (Case II in LTP), the injected Cu<sup>2+</sup> ions contribute not only to an increase in the conductance of the S-DNA electrolyte but also to further growth of the Cu filament,<sup>[50]</sup> thereby increasing the total conductance value more rapidly. This contribution of the Cu filament to the conductance change therefore provides the negative LTP nonlinearity ( $\alpha_p < 0$ ). When a series of inhibitory pulses (from 1st to 7th) is applied, a Joule heating-assisted oxidation process ( $\text{Cu} \rightarrow \text{Cu}^{2+} + 2\text{e}^-$ ) causes the dissolution of the Cu filament, resulting in an exponential decrease in conductance (Case II in LTD).<sup>[49,50]</sup> After the Cu filament



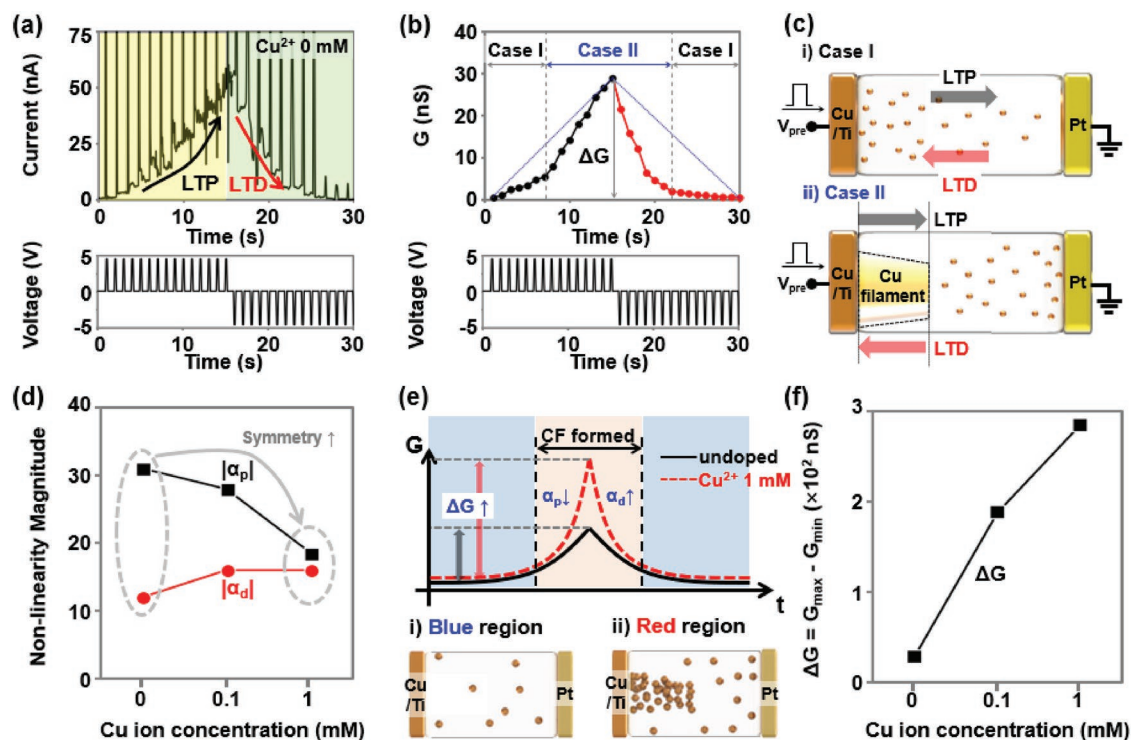


**Figure 2.** a) Current and b) conductance values of the undoped S-DNA device as a function of time, where 15 excitatory/inhibitory voltage pulses ( $V_{pre} = \pm 4.5$  V,  $f = 1$  Hz, and  $t_d = 100$  ms) were continuously applied to investigate the LTP/LTD characteristics. c) Schematics of  $\text{Cu}^{2+}$  diffusion (Case I) and conduction filament growth/decomposition (Case II) in the S-DNA device due to applying presynaptic voltage pulses. d) Magnitude of nonlinearity for LTP ( $\alpha_p$ ) and LTD ( $\alpha_d$ ) as a function of  $\text{Cu}^{2+}$  concentration (0, 0.1, and  $1 \times 10^{-3}$  M). e) LTP/LTD profiles of undoped/ $\text{Cu}^{2+}$ -doped S-DNA devices and a schematic showing the S-DNA before (blue region) and after (red region) the formation of conduction filaments. f) Weight update margin in the LTP/LTD curves as a function of  $\text{Cu}^{2+}$  concentration (0, 0.1, and  $1 \times 10^{-3}$  M).

completely disappears, the inhibitory pulse induces the diffusion of  $\text{Cu}^{2+}$  toward the Cu-side (Case I in LTD) and the diffused  $\text{Cu}^{2+}$  ions are trapped at the Cu/S-DNA interface.<sup>[49]</sup> This reduces the amount of  $\text{Cu}^{2+}$  in the S-DNA electrolyte gradually as an inhibitory pulse is supplied, finally leading to a linear decrease in conductance. In particular, the magnitude of the nonlinearity factors for the LTP and LTD curves varied oppositely when the S-DNA electrolyte was doped with a higher  $\text{Cu}^{2+}$  concentration. As shown in Figure 2d,  $|\alpha_p|$  reduced as the  $\text{Cu}^{2+}$  concentration increased from 0 to  $1 \times 10^{-3}$  M ( $|\alpha_p|$ : 31  $\rightarrow$  20), whereas  $|\alpha_d|$  increased from 12 to 18. This can be explained by the increase of the  $\text{Cu}^{2+}$  concentration in the S-DNA electrolyte. Before the formation of the Cu filament (LTP-side blue region in Figure 2e), the conductance change is only determined by the amount of  $\text{Cu}^{2+}$  ions injected from the Cu electrode. Thus, the conductance is not that different before/after  $\text{Cu}^{2+}$  doping (undoped: 6.2 nS,  $1 \times 10^{-3}$  M  $\text{Cu}^{2+}$ -doped: 18.4 nS). However, after the Cu filament partially forms, additionally supplied  $\text{Cu}^{2+}$  ions are predicted to help the growth of the Cu filaments (LTP-side red region).<sup>[50]</sup> These  $\text{Cu}^{2+}$  ions thicken the Cu filament, unlike in the control S-DNA device, resulting in a large conductance change (undoped: 27.7 nS,  $1 \times 10^{-3}$  M  $\text{Cu}^{2+}$ -doped: 268.6 nS). Similar conductance change is expected in the LTD-side two regions with (red) or without (blue) a Cu filament. Consequently, the  $1 \times 10^{-3}$  M  $\text{Cu}^{2+}$ -doped S-DNA device showed favorably symmetric LTP/LTD characteristics ( $\alpha_p$ :  $-20/\alpha_d$ : 18). The weight update margin ( $\Delta G$ ) was also dependent on the

$\text{Cu}^{2+}$  doping concentration. By increasing the  $\text{Cu}^{2+}$  concentration from 0 to  $1 \times 10^{-3}$  M,  $\Delta G$  was improved by factors of 8.2 ( $\Delta G$ : 33  $\rightarrow$  287 nS), as seen in Figure 2f.

We also found that the operating mode of the S-DNA device can convert from synapse to neuron by adjusting the duration time ( $t_d$ ) of voltage stimulus pulse. Figure 3a shows the current of the S-DNA device as a function of time, where a positive voltage pulse was applied repeatedly ( $V_{pre} = 4.5$  V,  $f = 1$  Hz). Like in the previous case in which a short voltage pulse with  $t_d = 50$  ms was applied, the current of the S-DNA device gradually increased as pulses with  $t_d = 100$  ms were supplied continuously ( $I = 157$  nA after applying the tenth pulse), representing long term plasticity. The increment in the current became larger when the duration time increased to 500 ms ( $I = 1.19$   $\mu$ A after applying the seventh pulse), and most of the increased current disappeared after the eighth pulse. This phenomenon indicates that the S-DNA device can operate as a neuron on the basis of two mechanisms: i) “integrating” electrical input signals and ii) “firing” electrical output signals when the integrated value exceeds a threshold point. This device-mode conversion from synapse to neuron was possible by virtue of the difference in growth rate of the Cu filament, which was dependent on the  $t_d$  of an input pulse. During the operation of the S-DNA device, the amount of diffused  $\text{Cu}^{2+}$  ions is proportional to the energy ( $V_{pre} \times t_d$ ), which is related to the applied voltage pulse.<sup>[51]</sup> When a lower-energy voltage pulse was applied ( $t_d = 100$  ms), the Cu filament grew slowly owing to the

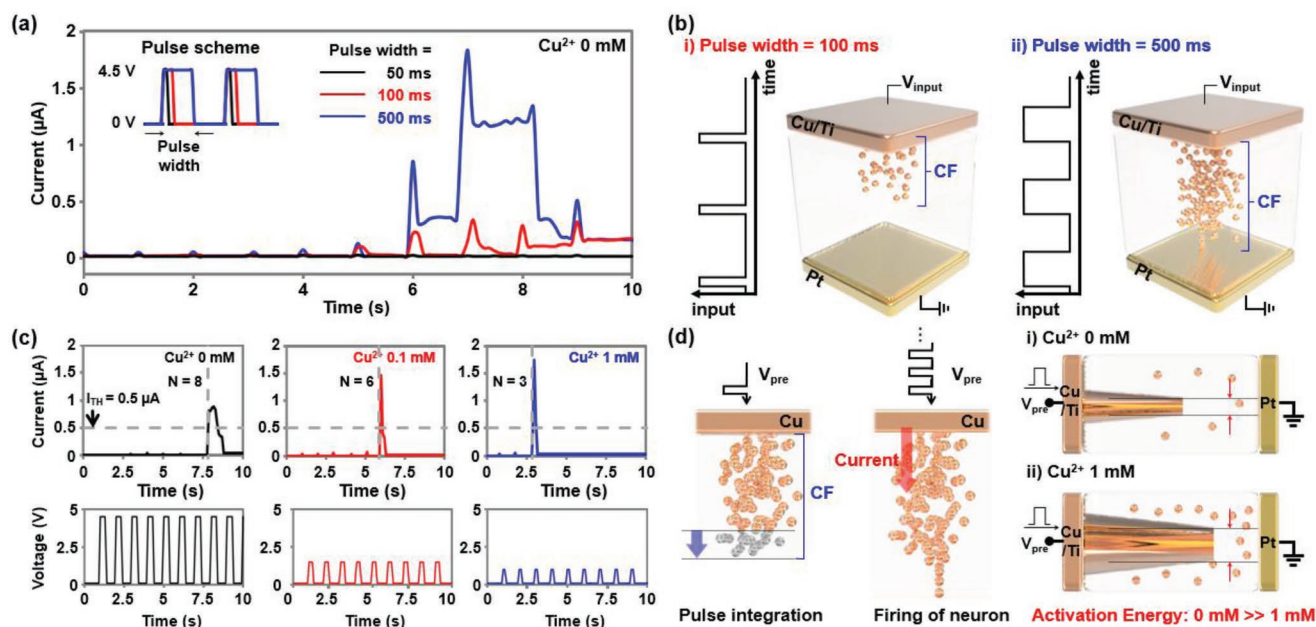


**Figure 3.** a) Current–time graph of the undoped S-DNA device with the application of a series of potentiation voltage pulses ( $V_{pre} = 4.5$  V,  $f = 1$  Hz) with various duration times of 50 (black), 100 (red), and 500 ms (blue). b) Schematic showing conducting filament formation according to different pulse duration times:  $t_d = 100$  ms (left) and  $t_d = 500$  ms (right). c) Current–time graphs of  $0 \times 10^{-3}$  M (left),  $0.1 \times 10^{-3}$  M (middle), and  $1 \times 10^{-3}$  M (right)  $\text{Cu}^{2+}$ -doped S-DNA devices with the application of a series of potentiation voltage pulses ( $V_{pre} = 4.5$ , 1.5, and 1 V for 0, 0.1, and  $1 \times 10^{-3}$  M  $\text{Cu}^{2+}$ -doped S-DNA devices, respectively). Here, the frequency and duration time of the voltage pulses were 1 Hz and 100 ms, respectively. d) Schematic showing the operating mechanism of the S-DNA neuron device (left) and the conducting filament formation in the S-DNA neuron devices fabricated on  $0 \times 10^{-3}$  M (right top) and  $1 \times 10^{-3}$  M (right bottom)  $\text{Cu}^{2+}$ -doped electrolytes.

decreased supply of  $\text{Cu}^{2+}$ , resulting in a small increase in the current (refer to the left panel of Figure 3b). Conversely, in the case of a higher-energy pulse ( $t_d = 500$  ms), a higher supply of  $\text{Cu}^{2+}$  accelerated the growth of the Cu filament. This rapidly grown Cu filament reached the Cu electrode, suddenly generating a spiking current (right panel of Figure 3b). However, this imperfect Cu filament spontaneously dissolved and the conductance of the S-DNA device returned to its initial level. This current firing phenomenon was more apparent with increasing  $\text{Cu}^{2+}$  concentration in the S-DNA electrolyte. Figure 3c presents the electrical characteristics of S-DNA devices doped with solutions with different  $\text{Cu}^{2+}$  concentrations (0, 0.1, and  $1 \times 10^{-3}$  M). Here, the positive voltage pulses with amplitudes of 4.5, 1.5, and 1 V, which were the same as the EPSC pulses used in the Figure 2 and Figure S4 in the Supporting Information, were applied to the 0, 0.1, and  $1 \times 10^{-3}$  M  $\text{Cu}^{2+}$ -doped S-DNA devices, respectively. The threshold current level for firing was set as  $0.5 \mu\text{A}$ . In the control device ( $\text{Cu}^{2+} 0 \times 10^{-3}$  M), an output current signal was fired after a +4.5 V voltage pulse was supplied eight times ( $N = 8$ ), where the peak current at the firing state was  $\approx 1 \mu\text{A}$ . After doping the S-DNA device with  $0.1 \times 10^{-3}$  M  $\text{Cu}^{2+}$ , the output current signal was fired early after the sixth input pulse ( $N = 6$ ), showing a higher peak current of  $1.5 \mu\text{A}$ . The peak current in firing increased up to  $1.8 \mu\text{A}$  and the number of voltage pulses required for firing reduced to  $N = 3$  by doping the device with  $1 \times 10^{-3}$  M of  $\text{Cu}^{2+}$ . This is attributed to the reduction in activation energy required for neuron firing owing to an increase in  $\text{Cu}^{2+}$  concentration. Figure 3d describes the neuron operation of the S-DNA device in the  $0 \times 10^{-3}$  M

(control) and  $1 \times 10^{-3}$  M  $\text{Cu}^{2+}$  doping conditions. When presynaptic voltage pulses are supplied continuously, Cu ions steadily stick to the Cu filament (pulse integration), eventually generating a spiking current pulse instantly (firing of neuron). From the neuron operating point of view,  $\text{Cu}^{2+}$  doping allowed for a relatively low amplitude of presynaptic voltage pulse ( $V_{0mM} > V_{1mM}$ ) and a low number of pulses for neuron firing ( $N_{0mM} > N_{1mM}$ ). Here, after the initial firing occurred, the S-DNA neuronal device did not show the firing phenomenon again. This is likely due to the nonvolatile characteristic of Cu conduction filament formed in S-DNA electrolyte. To remedy this shortcoming, it is necessary to initialize the Cu conductive filament with the assistance of external electrical element or circuit. For instance, Wang et al.<sup>[41]</sup> suggested a combination of a diffusive memristor ( $\text{Ag}/\text{SiO}_2/\text{Ag}/\text{Ag}$ ) and an external electrical component (e.g., capacitor) to achieve a leaky integrate-and-fire behavior and a persistent firing of neuron device.

With the S-DNA synaptic devices, we virtually constructed an online learning platform based on single- and multilayer artificial neural networks (ANNs), as shown in Figure 4a. For the pattern recognition simulation, we used the MNIST handwritten image dataset containing: i) 60 000 learning images and ii) 10 000 testing images that do not overlap with the learning dataset. The input and output layers of the platform were configured with 784 presynaptic neurons matching with  $28 \times 28$  array pixels of the MNIST images and 10 postsynaptic neurons corresponding to numbers “0” to “9.” Thus, 7840 pairs of potentiation and depression synapses ( $G^+$  and  $G^-$ ) were connected between the presynaptic and postsynaptic neurons; we

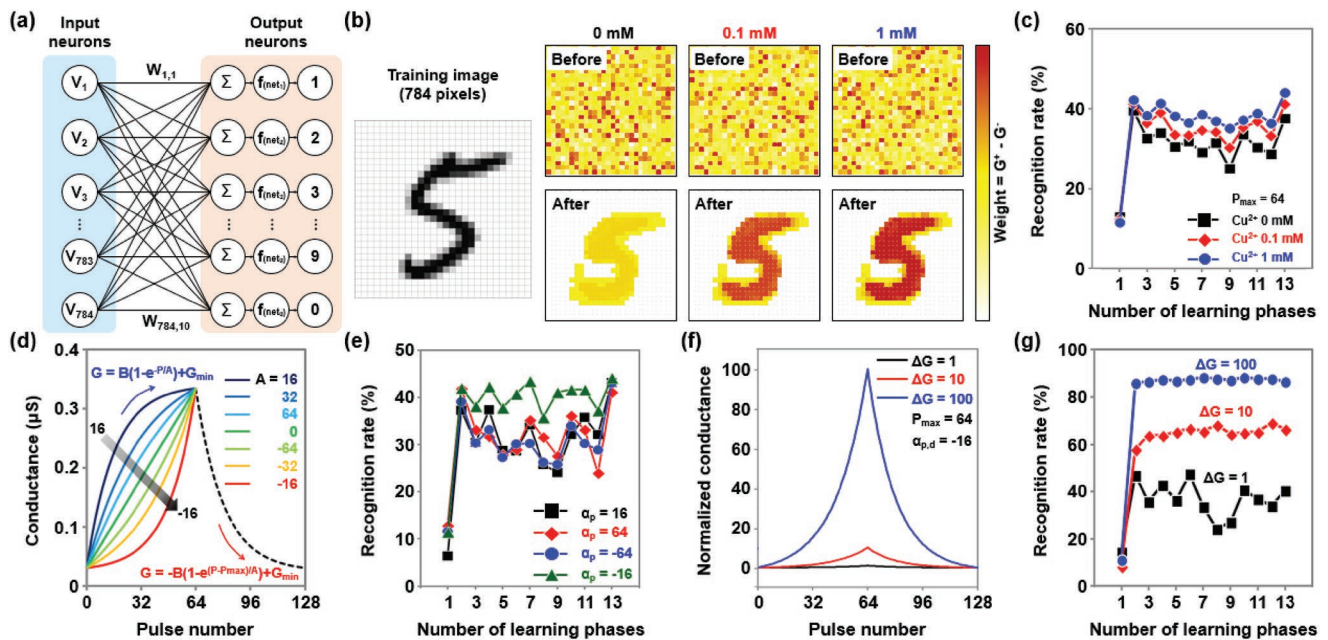


**Figure 4.** a) Online learning platform using single-layer perceptron-based ANN for MNIST pattern recognition. b) The weight mapping images of 784 synaptic weights for number “5” in three cases: 0, 0.1, and  $1 \times 10^{-3}$  M  $\text{Cu}^{2+}$ -doped S-DNA. c) Average recognition rates versus the number of learning phases for the three cases. d) LTP curves with various LTP nonlinearity values between  $-16$  and  $16$ , in which the following parameters were fixed: LTD nonlinearity ( $-16$ ), number of states ( $P_{\max} = 64$ ), and synaptic weight margin ( $\Delta G = 10$ ). e) Average recognition rates versus the number of learning phases for cases with  $\alpha_p = 16$  (black),  $64$  (red),  $-64$  (blue), and  $-16$  (green). f) LTP/LTD curves with different magnitudes of  $\Delta G$ :  $1$  (black),  $10$  (red), and  $100$  (blue). Here, the following parameters were fixed: LTP/LTD nonlinearity ( $\alpha_p = -16$ ,  $\alpha_d = -16$ ), number of states ( $P_{\max} = 64$ ), and on/off-current ratio ( $I_{\text{on}}/I_{\text{off}} = 10$ ) g) Average recognition rates versus number of learning phases for cases of  $\Delta G = 1$  (black),  $10$  (red), and  $100$  (blue).

calculated synaptic weight as  $W = G^+ - G^-$ . After the MNIST image data ( $V_1 - V_{784}$ ,  $V$ ) were transmitted to the input layer, they generated the postsynaptic current vector ( $I = \sum V \times W$ ), which is a product of the image data vector and the synaptic weight vector ( $W_{1,1} - W_{784,10}$ ,  $W$ ). This postsynaptic current vector was then converted into an output vector ( $f_{\text{net}}$ ) through the sigmoid activation function. Finally, to update the synaptic weight, we calculated the difference ( $\delta$ ) between the output value of each output neuron ( $V_{\text{out}}$ ) and the label data of the MNIST dataset ( $V_{\text{label}}$ ). If the sign of the product of the  $\delta$  value and the input value ( $\text{sgn}(\delta \times V_i)$ ) was positive, the relevant synapses' weights were updated in an increasing direction and vice versa. In the case of  $\delta = 0$ , the synaptic weight did not change ( $\text{sgn}(\delta \times V_i) = 0$ ). The MNIST learning phase is described in more detail in Figure S6 in the Supporting Information. The mapping images of 784 synaptic weights for the number “5” are plotted in Figure 4b. We assumed that the mapping image had random weight values before the learning step. After learning the MNIST datasets completely, 784 pixels indicating synaptic weights presented a clear shape of the number “5” that was similar to the target image. Here, the filled pixels in the mapping image indicate that the corresponding synaptic devices have high weight values and vice versa. With an increase in the  $\text{Cu}^{2+}$  doping concentration, the shape of the number “5” appeared more clearly in the mapping image, in which the color of the filled pixels became darker. This means that the  $\text{Cu}^{2+}$  doping process successfully improved the learning performance of ANNs consisting of S-DNA devices. This improvement was possible owing to the negative LTP nonlinearity (thereby,

the symmetric LTP/LTD characteristics) and the high weight update margin, which were achieved by the  $\text{Cu}^{2+}$  doping. To analyze the performance of ANNs quantitatively with respect to various  $\text{Cu}^{2+}$  doping concentrations, we performed a supervised learning with the MNIST learning dataset and then predicted the recognition rate. The MNIST test phase is detailed in Figure S7 in the Supporting Information. The average recognition rate for every 5000 learning phases was plotted in Figure 4c for cases of 0, 0.1, and  $1 \times 10^{-3}$  M  $\text{Cu}^{2+}$  doping. As predicted, the recognition rate after 60 000 learning phases increased from 38% to 44% as the concentration of  $\text{Cu}^{2+}$  increased from 0 to  $1 \times 10^{-3}$  M. This improvement in recognition rate achieved by increasing  $\text{Cu}^{2+}$  concentration was also identified by the multilayer perceptron (MLP) model-based MNIST simulation. Here, the MLP-based MNIST simulation was conducted on the “+NeuroSim” platform,<sup>[52]</sup> which was designed on the basis of a three-layer perceptron model with 400 input neurons, 100 hidden layer neurons, and 10 output neurons. As shown in Figure S8 in the Supporting Information, the recognition rate after 60 000 learning phases improved from 89.42% to 91.61% as the  $\text{Cu}^{2+}$  concentration increased from 0 to  $1 \times 10^{-3}$  M. The maximum recognition rate in this study (91.61%) was higher than the values obtained by conventional ReRAM-based ANNs (10–73%), which was also comparable to the value predicted by the FeFET synaptic device ( $\approx 90\%$ ).

We then investigated how the LTP nonlinearity ( $\alpha_p$ ) and the weight update margin ( $\Delta G$ ) affect the recognition rate. The mathematical LTP/LTD model was built with the equations  $G = B(1 - e^{P/A}) + G_{\min}$  and  $G = -B(1 - e^{(P - P_{\max})/A}) + G_{\min}$ . Figure 4d



shows LTP/LTD characteristic curves based on the model in which the nonlinearity of LTP was varied from  $-16$  to  $16$  and that of LTD was fixed as  $\alpha_d = -16$  ( $P_{\max} = 64$  and  $\Delta G = 10$ ). The negative and positive LTP nonlinearity values respectively indicate the synaptic operations of the S-DNA device and typical ReRAM<sup>[23,24]</sup>/PCRAM<sup>[21,22]</sup> devices. We performed the MNIST simulation once again with various  $\alpha_p$  values ( $16$ ,  $64$ ,  $-64$ , and  $-16$ ) and then plotted the resulting recognition rates as a function of the learning phase in Figure 4e. Although  $\alpha_p$  was varied from  $16$  to  $-64$ , the recognition rate after learning with  $60\,000$  MNIST image data did not change much and just varied between  $32\%$  and  $36\%$ . However, for  $\alpha_p = -16$ , the recognition rate immediately improved up to  $\approx 42\%$ . This is because the synaptic weights continue to increase as pulse signals for potentiation are supplied, unlike in the case of the conventional LTP characteristic with a positive  $\alpha_p$  in which synaptic weights are saturated as the number of input pulses increases. In addition, the weight update margin ( $\Delta G$ ) also influenced the recognition rate. We prepared LTP/LTD curves with different magnitudes of  $\Delta G$ , with  $\Delta G = 1$ ,  $10$  for the undoped S-DNA device and  $\Delta G = 100$  for the  $\text{Cu}^{2+}$ -doped S-DNA device (Figure 4f). The following parameters were fixed;  $\alpha_p/\alpha_d = -16/16$ ,  $P_{\max} = 64$ , and  $I_{\text{on}}/I_{\text{off}} = 10$ . Then, by using the three LTP/LTD curves, we performed the MNIST simulation and predicted the recognition rates as a function of the learning phase, as shown in Figure 4g. After completing the MNIST learning process, the recognition rate improved from  $40\%$  to  $82\%$  when  $\Delta G$  increased from  $1$  to  $100$ . The negative LTP nonlinearity and high weight update margin influenced the highest and lowest synaptic weights after the full learning process was completed, thereby improving the recognition rate for MNIST patterns.<sup>[52]</sup>

In conclusion, we studied a salmon deoxyribonucleic acid (S-DNA)-based neuromorphic device operating as both a synapse and a neuron. The S-DNA synaptic and neural operations were based on Cu redox reactions ( $\text{Cu} \leftrightarrow \text{Cu}^{2+} + 2\text{e}^-$ ), where the operating mode of the device could be converted by adjusting the duration time ( $t_d$ ) of the voltage pulse. When a voltage pulse with a short duration time ( $t_d = 100$  ms) was applied, the device successfully emulated the synaptic function, such as LTP/LTD characteristic. In addition, as applying a voltage pulse with a long duration time ( $t_d$ ), the device worked as a neuron based on its “integrate-and-fire” behavior. In particular, the following remarkable enhancements in the synaptic characteristics were achieved by using the  $\text{Cu}^{2+}$  doping technique: i) improvement in the nonlinearity of the LTP characteristic ( $|\alpha_p|$ :  $31 \rightarrow 20$ ) and ii) increase in the weight update margin ( $\Delta G$ :  $35 \rightarrow 287$  nS). The  $\text{Cu}^{2+}$  doping also modulated the threshold conditions for the firing of the neuronal device: i) the amplitude of the presynaptic voltage pulse ( $V_{\text{pulse}}$ : between  $4.5$  and  $1$  V) and ii) the required number of pulses for neuron firing ( $N$ : between  $8$  and  $3$ ). This is because  $\text{Cu}^{2+}$  doping of the S-DNA electrolyte reduced the activation energy for the formation of the conduction filament. In addition, owing to the negative LTP nonlinearity (the symmetric LTP/LTD characteristic) and the high weight update margin, which were achieved by the  $\text{Cu}^{2+}$  doping, the MNIST pattern recognition rates improved from  $38\%$  to  $44\%$  (single-layer perceptron model) and from  $89.42\%$  to  $91.61\%$  (multilayer perceptron model) with an increase in the concentration of  $\text{Cu}^{2+}$  from  $0$  to  $1 \times 10^{-3}$  M.

## Experimental Section

**Preparation of the S-DNA Solution with  $\text{Cu}^{2+}$  and an S-DNA Thin Film:**  $0.1$  g of S-DNA (GEM Corporation, Shiga, Japan) was dissolved in  $10$  mL of deionized (DI) water to make an S-DNA solution. Then,  $0$ ,  $0.1$ , and  $1 \times 10^{-3}$  M of  $\text{Cu}^{2+}$  (i.e.,  $\text{Cu}(\text{NO}_3)_2$  purchased from Sigma Aldrich, St. Louis, USA) were added to the S-DNA solution, followed by magnetic stirring ( $1000$  rpm for  $24$  h at room temperature). For the formation of an S-DNA film,  $20$   $\mu\text{L}$  of the  $\text{Cu}^{2+}$ -doped S-DNA solution was spin-coated on an  $\text{SiO}_2/\text{Si}$  substrate at  $3000$  rpm for  $90$  s, and then the samples were annealed at  $100$  °C in a vacuum oven for  $2$  min. The illustration that describes this process is in Figure S1 in the Supporting Information. The thickness of S-DNA electrolyte was  $\approx 30$  nm (see Figure S9, Supporting Information), which was investigated by performing atomic force microscopy (ND-MDT, NTEGRA Spectra).

**Characterization of the  $\text{Cu}^{2+}$ -Doped S-DNA Thin Film:** The S-DNA thin films with different concentrations of  $\text{Cu}^{2+}$  ( $0$ ,  $0.1$ , and  $1 \times 10^{-3}$  M) were subjected to Raman spectroscopy (Alpha300 M+, WITec) and FT-IR (MIR\_ATR (ZnSe), Bruker Inc.) analysis. A Raman spectroscope with an excitation wavelength of  $532$  nm was used. The beam size of the laser was  $\approx 0.7$ – $0.9$   $\mu\text{m}$ , and the instrumental spectral resolution was less than  $0.9$   $\text{cm}^{-1}$ . The FT-IR spectral range was from  $600$  to  $3700$   $\text{cm}^{-1}$ , the scan rate was  $32$  scans per s, and the resolution was  $\approx 4$   $\text{cm}^{-1}$ . To analyze the FT-IR data, we subtracted the background spectrum produced by bare glass.

**Fabrication of the S-DNA Neuromorphic Device:** The surface of the  $\text{SiO}_2$  substrate was cleaned through a sonication process for  $10$  min in acetone, 2-propanol, and deionized water. A bottom electrode with Pt ( $10$  nm) and Ti ( $5$  nm) was formed on the  $\text{SiO}_2$  substrate using an e-beam evaporator and a shadow mask (5-line pattern, and each line width was  $100$   $\mu\text{m}$ ). After coating a  $20$  nm thick S-DNA film on the Pt/Ti/ $\text{SiO}_2$  sample, a top electrode with Cu ( $30$  nm) and Ti ( $2.5$  nm) was deposited using the same shadow mask with the 5-line pattern.

**Characterization of the S-DNA Neuromorphic Device:** The fabricated S-DNA devices were electrically analyzed by using a semiconductor parameter analyzer (HP-4155A) connected with a voltage pulse generator (Keysight, 33500B). The measurement set up is described in Figure S2 in the Supporting Information. To read the current flowing between pre- and postsynaptic terminals, a constant voltage of  $0.1$  V was applied to a presynaptic terminal. To analyze synaptic characteristics, a series of  $15$  excitatory/inhibitory pulses ( $t_d = 100$  ms) was applied to a presynaptic terminal;  $V_{\text{pre}}$  were  $\pm 4.5$ ,  $\pm 1.5$ , and  $\pm 1$  V for the  $0$ ,  $0.1$ , and  $1 \times 10^{-3}$  M  $\text{Cu}^{2+}$ -doped S-DNA devices, respectively. To investigate the neural characteristics of S-DNA devices, a series of potentiation pulses ( $t_d = 500$  ms) was used. Here, the values of  $V_{\text{pre}}$  were the same as the values used for synapse characterization.

## Supporting Information

Supporting Information is available from the Wiley Online Library or from the author.

## Acknowledgements

D.-H.K. and J.-H.K. contributed equally to this work. This research was supported by the Basic Science Research Program, Basic Research Lab Program, and Nano-Material Technology Development Program through the National Research Foundation of Korea (NRF) grants funded by the Korea government (MSIP) (2018R1A2A2A05020475, 2017R1A4A1015400, and 2016M3A7B4910426, 2015M3A7B7045496), and the Future Semiconductor Device Technology Development Program (10067739) funded by the Ministry of Trade, Industry and Energy (MOTIE), and Korea Semiconductor Research Consortium (KSRC).

Note: The equal contribution statement was added on September 4, 2019 after initial online publication.

## Conflict of Interest

The authors declare no conflict of interest.

## Keywords

handwritten digit pattern recognition, neural devices, neuromorphic devices, salmon DNA, synaptic devices

Received: May 27, 2019  
Published online: July 15, 2019

- [1] S. Kim, B. Choi, M. Lim, Y. Kim, H. D. Kim, S. J. Choi, *Small* **2018**, *14*, 1800521.
- [2] P. Yao, H. Q. Wu, B. Gao, S. B. Eryilmaz, X. Y. Huang, W. Q. Zhang, Q. T. Zhang, N. Deng, L. P. Shi, H. S. P. Wong, H. Qian, *Nat. Commun.* **2017**, *8*, 15199.
- [3] J. Hur, B. C. Jang, J. Park, D. I. Moon, H. Bae, J. Y. Park, G. H. Kim, S. B. Jeon, M. Seo, S. Kim, *Adv. Funct. Mater.* **2018**, *28*, 1804844.
- [4] S. Yu, D. Kuzum, H.-S. P. Wong, in *2014 IEEE International Symposium on Circuits and Systems (ISCAS)*, IEEE, Piscataway, NJ, USA **2014**, pp. 1062–1065.
- [5] D. Kuzum, R. G. Jeyasingh, H.-S. P. Wong, in *2011 International Electron Devices Meeting*, IEEE, Piscataway, NJ, USA **2011**, pp. 30.3.1–30.3.4.
- [6] S. Lim, J.-H. Bae, J.-H. Eum, S. Lee, C.-H. Kim, D. Kwon, J.-H. Lee, in *2018 IEEE International Symposium on Circuits and Systems (ISCAS)*, IEEE, Piscataway, NJ, USA **2018**, pp. 1–5, <https://doi.org/10.1109/ISCAS.2018.8351152>.
- [7] H. Kim, S. Hwang, J. Park, B.-G. Park, *Nanotechnology* **2017**, *28*, 405202.
- [8] C. Yang, H. Kim, S. P. Adhikari, L. O. Chua, *Sensors* **2016**, *17*, 16.
- [9] P. Stoliar, J. Tranchant, B. Corraze, E. Janod, M. P. Besland, F. Tesler, M. Rozenberg, L. Cario, *Adv. Funct. Mater.* **2017**, *27*, 1604740.
- [10] S. Kim, B. Choi, M. Lim, J. Yoon, J. Lee, H.-D. Kim, S.-J. Choi, *ACS Nano* **2017**, *11*, 2814.
- [11] S. Seo, S.-H. Jo, S. Kim, J. Shim, S. Oh, J.-H. Kim, K. Heo, J.-W. Choi, C. Choi, S. Oh, D. Kuzum, H. S. P. Wong, J.-H. Park, *Nat. Commun.* **2018**, *9*, 5106.
- [12] J.-S. Seo, B. Brezzo, Y. Liu, B. D. Parker, S. K. Esser, R. K. Montoye, B. Rajendran, J. A. Tierno, L. Chang, D. S. Modha, in *2011 IEEE Custom Integrated Circuits Conference (CICC)*, IEEE, Piscataway, NJ, USA **2011**, pp. 1–4, <https://doi.org/10.1109/CICC.2011.6055293>.
- [13] N. Qiao, H. Mostafa, F. Corradi, M. Osswald, F. Stefanini, D. Sumislawska, G. Indiveri, *Front. Neurosci.* **2015**, *9*, 141.
- [14] J.-S. Seo, M. Seok, in *2015 IFIP/IEEE International Conference on Very Large-Scale Integration (VLSI-SoC)*, IEEE, Piscataway, NJ, USA **2015**, pp. 49–51.
- [15] M.-W. Kwon, M.-H. Baek, J. Park, H. Kim, S. Hwang, B.-G. Park, *J. Semicond. Tech. Sci.* **2017**, *17*, 174.
- [16] D. Kuzum, R. G. Jeyasingh, B. Lee, H.-S. P. Wong, *Nano Lett.* **2012**, *12*, 2179.
- [17] R. Wojtyna, T. Talaska, *Tech. Sci.* **2006**, *54*, 443.
- [18] J.-H. Bae, S. Lim, B.-G. Park, J.-H. Lee, *IEEE Electron Device Lett.* **2017**, *38*, 1153.
- [19] S. Kim, J. Yoon, H.-D. Kim, S.-J. Choi, *ACS Appl. Mater. Interfaces* **2015**, *7*, 25479.
- [20] S. H. Jo, T. Chang, I. Ebong, B. B. Bhadviya, P. Mazumder, W. Lu, *Nano Lett.* **2010**, *10*, 1297.
- [21] M. Suri, V. Sousa, L. Perniola, D. Vuillaume, B. DeSalvo, in *The 2011 International Joint Conference on Neural Networks*, IEEE, Piscataway, NJ, USA **2011**, pp. 619–624.
- [22] M. Suri, O. Bichler, D. Querlioz, O. Cueto, L. Perniola, V. Sousa, D. Vuillaume, C. Gamrat, B. DeSalvo, in *2011 International Electron Devices Meeting*, IEEE, Piscataway, NJ, USA **2011**, pp. 4.4.1–4.4.4.
- [23] S. Yu, B. Gao, Z. Fang, H. Yu, J. Kang, H.-S. P. Wong, in *2012 International Electron Devices Meeting*, IEEE, Piscataway, NJ, USA **2012**, pp. 10.4.1–10.4.4.
- [24] S. Yu, B. Gao, Z. Fang, H. Yu, J. Kang, H. S. P. Wong, *Adv. Mater.* **2013**, *25*, 1774.
- [25] K. Seo, I. Kim, S. Jung, M. Jo, S. Park, J. Park, J. Shin, K. P. Biju, J. Kong, K. Lee, *Nanotechnology* **2011**, *22*, 254023.
- [26] X. Zhang, S. Liu, X. Zhao, F. Wu, Q. Wu, W. Wang, R. Cao, Y. Fang, H. Lv, S. Long, *IEEE Electron Device Lett.* **2017**, *38*, 1208.
- [27] A. Nayak, T. Ohno, T. Tsuruoka, K. Terabe, T. Hasegawa, J. K. Gimzewski, M. Aono, *Adv. Funct. Mater.* **2012**, *22*, 3606.
- [28] S. Park, J. Noh, M.-I. Choo, A. M. Sheri, M. Chang, Y.-B. Kim, C. J. Kim, M. Jeon, B.-G. Lee, B. H. Lee, *Nanotechnology* **2013**, *24*, 384009.
- [29] P.-Y. Chen, L. Gao, S. Yu, *IEEE Trans. Multi-Scale Comput. Syst.* **2016**, *2*, 257.
- [30] P. Huang, D. Zhu, S. Chen, Z. Zhou, Z. Chen, B. Gao, L. Liu, X. Liu, J. Kang, *IEEE Trans. Electron Devices* **2017**, *64*, 614.
- [31] S. Kim, Y. Abbas, Y.-R. Jeon, A. S. Sokolov, B. Ku, C. Choi, *Nanotechnology* **2018**, *29*, 415204.
- [32] A. Chiolerio, M. Chiappalone, P. Ariano, S. Bocchini, *Front. Neurosci.* **2017**, *11*, 70.
- [33] J. Park, M. Kwak, K. Moon, J. Woo, D. Lee, H. Hwang, *IEEE Electron Device Lett.* **2016**, *37*, 1559.
- [34] R. Berdan, E. Vasilaki, A. Khiat, G. Indiveri, A. Serb, T. Prodromakis, *Sci. Rep.* **2016**, *6*, 18639.
- [35] W. Wang, D. Loke, L. Law, L. Shi, R. Zhao, M. Li, L. Chen, H. Yang, Y. Yeo, A. Adeyeye, in *2012 International Electron Devices Meeting*, IEEE, Piscataway, NJ, USA **2012**, pp. 31.3.1–31.3.4.
- [36] C. D. Wright, Y. Liu, K. I. Kohary, M. M. Aziz, R. J. Hicken, *Adv. Mater.* **2011**, *23*, 3408.
- [37] R. Naous, M. AlShedivat, E. Neftci, G. Cauwenberghs, K. N. Salama, *AIP Adv.* **2016**, *6*, 111304.
- [38] M. Prezioso, I. Kataeva, F. Merrikh-Bayat, B. Hoskins, G. Adam, T. Sota, K. Likharev, D. Strukov, in *2015 IEEE International Electron Devices Meeting (IEDM)*, IEEE, Piscataway, NJ, USA **2015**, pp. 17.4.1–17.4.4.
- [39] T. Tuma, A. Pantazi, M. Le Gallo, A. Sebastian, E. Eleftheriou, *Nat. Nanotechnol.* **2016**, *11*, 693.
- [40] C. Adda, B. Corraze, P. Stoliar, P. Diener, J. Tranchant, A. Filatre-Furcate, M. Fourmigué, D. Lorcy, M.-P. Besland, E. Janod, *J. Appl. Phys.* **2018**, *124*, 152124.
- [41] Z. Wang, S. Joshi, S. Savel'ev, W. Song, R. Midya, Y. Li, M. Rao, P. Yan, S. Asapu, Y. Zhuo, H. Jiang, P. Lin, C. Li, J. H. Yoon, N. K. Upadhyay, J. Zhang, M. Hu, J. P. Strachan, M. Barnell, Q. Wu, H. Wu, R. S. Williams, Q. Xia, J. J. Yang, *Nat. Electron.* **2018**, *1*, 137.
- [42] J. Sun, S. Oh, Y. Choi, S. Seo, M. J. Oh, M. Lee, W. B. Lee, P. J. Yoo, J. H. Cho, J.-H. Park, *Adv. Funct. Mater.* **2018**, *28*, 1804397.
- [43] L.-G. Wang, W. Zhang, Y. Chen, Y.-Q. Cao, A.-D. Li, D. Wu, *Nanoscale Res. Lett.* **2017**, *12*, 65.
- [44] C. Wu, T. W. Kim, H. Y. Choi, D. B. Strukov, J. J. Yang, *Nat. Commun.* **2017**, *8*, 752.
- [45] B. Attarimashalkoubek, A. Prakash, S. Lee, J. Song, J. Woo, S. H. Misha, N. Tamanna, H. Hwang, *ECS Solid State Lett.* **2014**, *3*, P120.
- [46] B. Gnappareddy, T. Ha, S. R. Dugasani, J. A. Kim, B. Kim, T. Kim, J. H. Kim, S. H. Park, *RSC Adv.* **2015**, *5*, 39409.
- [47] M. Vasudev, T.-C. Wu, S. Biswas, M. Dutta, M. A. Stroschio, S. Guthrie, M. Reed, K. P. Burris, C. Stewart Jr., *IEEE Trans. Nanotechnol.* **2011**, *10*, 35.
- [48] S. R. Dugasani, B. Paulson, T. Ha, T. S. Jung, B. Gnappareddy, J. A. Kim, T. Kim, H. J. Kim, J. H. Kim, K. Oh, *J. Phys. D: Appl. Phys.* **2018**, *51*, 285301.
- [49] S. Wu, T. Tsuruoka, K. Terabe, T. Hasegawa, J. P. Hill, K. Ariga, M. Aono, *Adv. Funct. Mater.* **2011**, *21*, 93.
- [50] K. Krishnan, T. Tsuruoka, C. Mannequin, M. Aono, *Adv. Mater.* **2016**, *28*, 640.
- [51] M. Suri, D. Querlioz, O. Bichler, G. Palma, E. Vianello, D. Vuillaume, C. Gamrat, B. DeSalvo, *IEEE Trans. Electron Devices* **2013**, *60*, 2402.
- [52] P.-Y. Chen, X. Peng, S. Yu, in *2017 IEEE International Electron Devices Meeting (IEDM)*, IEEE, Piscataway, NJ, USA **2017**, pp. 6.1.1–6.1.4.